Surface reconstruction of Pt(001) quantitatively revisited

R. Hammer,[1] K. Meinel,[1] O. Krahn,[1] and W. Widdra[1,2,*]
[1]*Institute of Physics, Martin-Luther-Universität Halle-Wittenberg, D-06099 Halle, Germany*
[2]*Max-Planck Institut für Mikrostrukturphysik, D-06120 Halle, Germany*
(Received 12 July 2016; published 7 November 2016)

The complex hexagonal reconstructions of the (001) surfaces of platinum and gold have been under debate for decades. Here, the structural details of the Pt(001) reconstruction have been quantitatively reinvestigated by combining the high resolving power of scanning tunneling microscopy (STM) and spot profile analysis low energy electron diffraction (SPA-LEED). In addition, LEED simulations based on a Moiré approach have been applied. Annealing temperatures around 850 °C yield a superstructure that approaches a commensurable $c(26.6 \times 118)$ substrate registry. It evolves from a Moiré-like buckling of a compressed hexagonal top layer (hex) where atomic rows of the hex run parallel to atomic rows of the square substrate. Annealing at 920 °C stimulates a continuous rotation of the hex where all angles between $\pm 0.7°$ are simultaneously realized. At temperatures around 1080 °C, the nonrotated hex coexists with a hex that is rotated by about 0.75°. Annealing at temperatures around 1120 °C yield a locking of the hex in fixed rotation angles of 0.77°, 0.88°, and 0.94°. At temperatures around 1170 °C, the Pt(001)-hex-*R* 0.94° prevails as the energetically most favored form of the rotated hex.

DOI: 10.1103/PhysRevB.94.195406

I. INTRODUCTION

The (001) surfaces of the late 5*d* transition metals Ir, Au, and Pt display a characteristic reconstruction where the top layer is compressed and show a pseudohexagonal ordering instead of a square lattice. First deduced from conventional low energy electron diffraction (LEED) studies [1–6], the hexagonal top layer (hex) reconstructions of Ir, Au, and Pt have been intensively studied over the last decades by applying almost the entire arsenal of surface analysis techniques. Besides diffraction using electrons [1–24], x rays [25,26], or He atoms [27,28] high-resolution real space investigations by means of scanning tunneling microscopy (STM) [24,29–33], electron reflection microscopy [34–36], electron transmission microscopy [37–39], field ion microscopy [40], and low energy electron microscopy [41] also have been employed. Additionally, there exists a series of theoretical approaches [24,42–46]. One of the main issues of these theoretical studies is the finding that for a free-standing Au monolayer the relativistically enhanced *d*-*d* hybridization yields a strong compression, which is the main reason for the hexagonal reordering of the top layers of Ir(001), Au(001), and Pt(001) [44,46]. The enormous interest for the hex reconstruction is not only induced by reasons of basic research. It is also motivated by the widespread technological impacts of those elements including, e.g., catalytic reactions [47–49], electrochemical processes [50–52], formation of nanostructures [53–55], or atomic surface transport [39,56–60].

Despite scientific efforts, a detailed understanding of the hex reconstruction has not been completely achieved up to now. Certainly, for the Ir(001)-hex a relatively simple (1×5) unit cell of the superstructure has been derived already in early studies [6,7]. For the Au(001)-hex and the Pt(001)-hex, however, the unit cells are much larger, which hampers their exact measurement by conventional diffraction techniques. Several studies report for Au and Pt $(5 \times N)$ reconstructions where $N = 20$–30 [2,4,14,15,22]. In addition, centered unit cells have also been taken into account. Whereas for the Au(001) reconstruction a $c(26 \times 68)$ structure or a $c(26 \times 48)$ structure was proposed by van Hove *et al.* [15] and by Binnig *et al.* [29], respectively, for the Pt(001)-hex Kuhnke *et al.* [28] estimated from He diffraction data a $c(26 \times 150)$ pattern. Moreover, there is a tendency of a slight rotation of the hex. In the case of Pt(001), $a \pm (0.7° \pm 0.2°)$ rotation was observed at temperatures above 850 °C [14]. The rotated Pt(001)-hex-*R* 0.7° was also described in matrix notation as $\binom{N\ 1}{1\ 5}$ structure, where $N = 12$–14 [19], and has been considered as the stable form of the Pt(001) reconstruction. The hex layer rotation, however, may locally vary, which induces a further handicap in structure elucidation. If high-resolution real space inspections by means of STM are performed, the question arises as to whether the observed structure characterizes merely the local situation or whether it really represents the sample in general. Hence, such real space investigations should be complemented by lateral averaging diffraction techniques of sufficient resolution in order to ensure that the obtained results are representative for the whole sample.

Recently, we combined the high-resolution power of STM and spot profile analysis LEED (SPA-LEED) [61,62] in order to perform a high precision analysis of the Au(001)-hex [63]. Whereas STM reveals the existence of several reconstruction types depending on local step density, SPA-LEED clearly showed the prevalence of one distinct hex structure. In combination with a Moiré approach for simulating the LEED data, this lead to a Moiré-like centered $c(28 \times 48)$ superstructure for the nonrotated Au(001)-hex, which is commensurate to the square (001) substrate. A slight disturbance of the surface structural order by means of Ar^+ ion bombardment at elevated temperatures induces an instable rotation of the hex layer up to angles of $\pm 0.83°$. During rotation, the internal structure of the hex remains fixed.

In the present paper, we focus on the Pt(001) reconstruction and use a combined STM and SPA-LEED analysis. In a first investigation, we analyze the nonrotated Pt(001)-hex, which shows up after annealing the sputtered sample at

*Corresponding author: wolf.widdra@physik.uni-halle.de

temperatures around 850 °C. The STM and the LEED reveal that a highly ordered hex structure is developed, approaching a commensurate $c(26 \times 118)$ superstructure. This structure, however, is metastable. Sample annealing at temperatures above 900 °C induces several variants of a rotated hex. Besides a continuous rotation of the hex over an angle area between 0 and $\pm 0.7^\circ$, fixed rotation angles of 0.77°, 0.88°, and 0.94° have been found. For the observed locking angles, point-on-line or line-on-line coincidences are attained where lattice lines of the hex match with lattice lines of the substrate. Such alignments may improve the hex to substrate matching and may yield minima in the hex-substrate interaction potential [64].

II. EXPERIMENT

The experiments have been performed in two ultra-high vacuum (UHV) systems (base pressure 1×10^{-10} mbar). One is equipped with a cylindrical mirror analyzer for Auger electron spectroscopy (AES), a room temperature (RT) STM (not used in this paper), and a commercial electron optic (Omicron) for SPA-LEED. The other chamber was exclusively used for the real space characterization of the Pt(001)-hex by means of STM. It contains a conventional LEED optic (Omicron) and a home-built low temperature STM working within a commercial Konti cryostat (Cryovac) at 77 K. In both systems, the usual facilities for sample cleaning via Ar^+ sputtering and annealing in O_2 atmosphere and UHV have been established. In the investigations, two Pt(001) crystals (Matek) with a miscut <0.2° have been employed. The crystals were mounted on Ta holders and cleaned *in situ* by cycles of 600 eV Ar^+ ion sputtering and shortly annealing (flashing) at temperatures of 1000 °C. Temperature has been measured with a pyrometer (Cyclops, AMETEK Land, UK). Sputtering ions stroke the samples at an angle of 45° with a current density of 3 μA/cm^2. Subsequently, annealing at 650 °C in O_2 atmosphere (1×10^{-6} mbar) was applied in order to remove C contamination. In the LEED studies, the sample was heated by a tungsten filament mounted behind the sample holder, which allowed heating by radiation and electron bombardment, respectively, up to temperatures of 1200 °C. Cleanliness and structural perfection of the surfaces were checked by AES and LEED. The cleaned samples displayed only the characteristic Auger signals of Pt, and LEED revealed the characteristic patterns of the Pt(001)-hex reconstruction. The measurements for the structure analysis were taken after a final annealing step performed at temperatures around 1000 °C and a short sputtering step taken after cooling down to RT. Afterward, the samples have been annealed in UHV. At temperatures around 850 °C, a high-quality nonrotated Pt(001)-hex developed, as indicated by brilliant and sharp LEED spots and the development of large terraces (step distances some 100 nm) as STM revealed. Annealing at higher temperatures yields different variants of the rotated Pt(001)-hex-$R\varphi$. In the LEED measurements, energies of 200 eV and 220 eV have been mainly used. At 200 eV, the spots of the unit cell of the hex induced Moiré superstructure were most brilliant, whereas at 220 eV the spots of the hex unit cell itself shines up most intensely. The same SPA-LEED parameters as in a former paper were used (transfer width better than 200 nm [62] and measured spot width 0.8% of Brillouin zone [63]). The LEED studies were initially taken at RT. As these studies require measuring times of several hours, the gradual decomposition of the Pt(001) reconstruction by CO [65] has been taken into account. The CO is coming from the residual gas pressure and is mainly released by the filaments. The CO problem has been solved by reducing all filament currents and by performing SPA-LEED at temperatures around 100 °C.

For attaining high-precision structure data, the characteristic barrel distortion of SPA-LEED has been corrected by using calibration samples of known structure with a high density of diffraction spots. Besides Si(111)-(7×7), which is adequate for hexagonal structures [66], we used also square structures of $BaTiO_3$ films on Pt(001) displaying oxygen vacancy structures such as (4×4),(8×8),$c(10 \times 10)$, and (10×10) variants [67] as well as TiO_2 films on Pt(001) showing a (4×13) ordering [68].

In the STM studies, the sample preparation follows essentially the procedure applied for the LEED investigations. However, for the sample annealing a boron nitride heater was used. Structural perfection and cleanliness of the sample have been checked by LEED and STM. Measurements started when STM reveals large and clean terraces with perfect hex layer structures. The STM has been performed in constant current mode after cooling down the sample to a temperature of 77 K. Similar to the LEED studies, filament currents have been reduced or switched off during measurements for reducing CO contamination.

III. RESULTS AND DISCUSSIONS

A. The nonrotated Pt(001)-hex

For introducing into the hexagonal reconstruction of Pt(001), a hard sphere model is shown in Fig. 1 in combination with a real space STM measurements of the hex. As visualized in the model, a two-dimensional hex layer is present on top of the square (1×1) substrate, in which the next neighbor distance is compressed by almost 4%, similar as for Au(001) [63]. The hex and the square substrate are characterized by the lattice vectors $\mathbf{a}_{1,2h}$ and $\mathbf{a}_{1,2q}$, respectively. Vectors $\mathbf{a}_{1h,1q}$ point to the [110] direction and run parallel to the closed packed atomic rows of the Pt(001)-(1×1) substrate. Vector $\mathbf{a}_{2h}$ is rotated by the angle $\varphi \approx 60^\circ$ from that direction. Due to the structural misfit, the hex atoms reside on the square substrate on different positions such as top, bridge, and hollow positions. Hence, the hex displays a Moiré-like height modulation. At top and hollow sites, respectively, ridges (R) and grooves (V) (see makers at the bottom of the model in Fig. 1) are formed along [110] with a distance of about $5|a_q|$, which shape the characteristic row pattern of the hex. Due to the compression of the hex, the atoms of the ridge alternately change from top to saddle positions, which induces a periodic splitting of the ridges. These characteristic features of the hex superstructure have been clearly revealed earlier by atomically resolved STM measurements of the Pt(001)-hex [31,32,58].

Since for the Pt(001)-hex a very large unit cell has to be expected [27], atomically resolved measurements are of restricted efficiency. Large-scale imaging is more adequate as it emphasizes the long-range modulations of the superstructure. In Fig. 2(a), such a large-scale STM image of a nonrotated

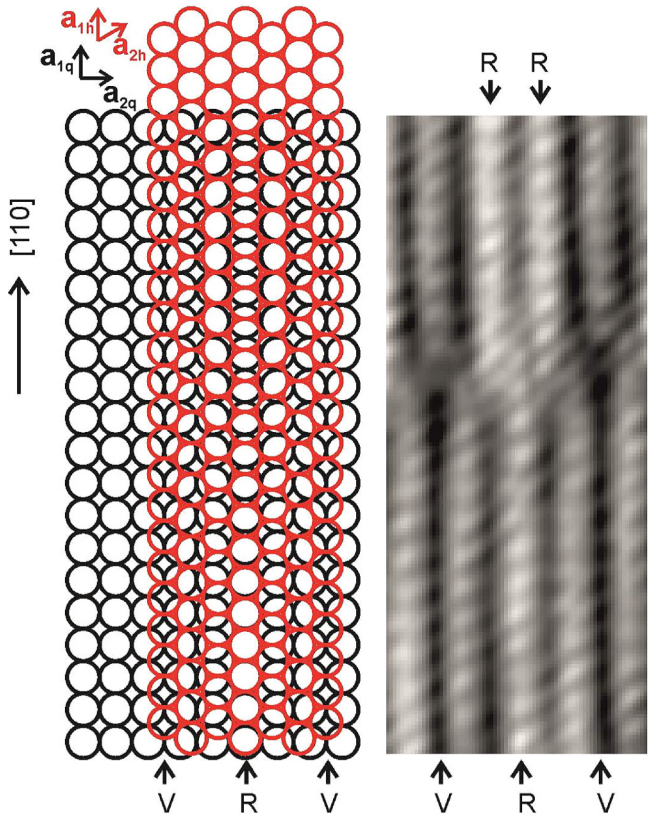

FIG. 1. Hard sphere model of the nonrotated hexagonal reconstruction of Pt(001) in combination with the STM image (2.2 × 5.5 nm^2,5 pA, − 0.5 V). Lattice vectors $\mathbf{a}_{1q}$ and $\mathbf{a}_{2q}$ of the square Pt(001)-(1 × 1) lattice (atoms in black) as well as $\mathbf{a}_{1h}$ and $\mathbf{a}_{2h}$ of the hex layer (atoms in red) are drawn as red and black arrows, respectively. The characteristic row pattern along [110] with ridges (R), where the hex atoms reside either on top and on bridge positions, and grooves (V), where the hex atoms reside either on hollow and on bridge positions, is indicated. Due to the change from top to bridge positions, a characteristic periodic splitting of the ridges occurs along [110].

Pt(001)-hex is displayed. It clearly shows the characteristic row pattern running along [110]. Besides the rows, one observes weak height modulations along, as well as perpendicular to, the reconstruction rows. These height modulations are related to the regular arrangement of identical hex sites (e.g., ideal on top positions). They define the lattice mesh of the hex-induced superstructure. One perceives that the lattice forms a rhomblike pattern similar as that for the Au(001)-hex [63]. Its unit cell is given by the dashed diamond in Fig. 2(a), which can be also described by a centered rectangular unit cell, shown in blue. The vectors $\mathbf{a}_s$ and $\mathbf{a}_l$ characterize its short and long sides, respectively.

In order to denominate a centered rectangular unit cell, a $c(2m \times 2n)$ notation is useful. The terms m and n result from the relations of the vectors $\mathbf{a}_l$ and $\mathbf{a}_s$ to the square Pt(001)-(1 × 1) lattice yielding

$$|\mathbf{a}_s|/|\mathbf{a}_q| = 2m \quad \text{and} \quad |\mathbf{a}_l|/|\mathbf{a}_q|. = 2n. \tag{1}$$

A rough estimation of m and n can be obtained by measuring the real space unit cell, as indicated in the STM

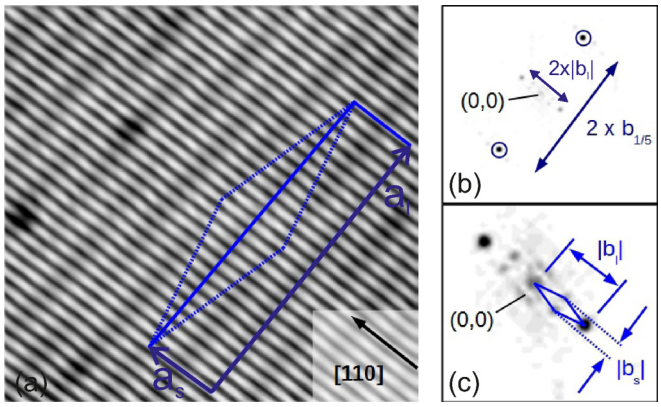

FIG. 2. (a) The STM image of the Pt(001)-hex (44 × 42 nm^2, 10 pA, −0.5 V) displaying the characteristic reconstruction rows along [110]. Blue dashed diamond and blue rectangle represent the centered $c(2m \times 2n)$ unit cell of the hex superstructure characterized by the vectors of $\mathbf{a}_s$ and $\mathbf{a}_l$. The FFT patterns of the STM image in (b) and (c) show the reciprocal space around the (0,0) diffraction spot at different magnifications. The (26 × 118) unit cell is indicated in (c) as a blue diamond. For details, see text.

image of Fig. 2(a). However, a more reliable result can be obtained from reciprocal space data. They can be extracted from the STM image by a fast Fourier transformation (FFT). The latter immediately yields an averaging over the periodic structure of the whole STM image. The FFT results are displayed in Figs. 2(b) and 2(c). The row induced spots that arise near one-fifth order positions of the reciprocal lattice of the square Pt(001)-(1 × 1) substrate are easily identified [encircled in Fig. 2(b)]. Inspecting the region around (0,0), one observes diamondlike spot constellations, which directly mark the unit cell of the hex superstructure in reciprocal space. It is described by the reciprocal lattice vectors $\mathbf{b}_l$ and $\mathbf{b}_s$ representing its long and the short side, respectively. They are ruled by the relations

$$|\mathbf{b}_l|/|\mathbf{b}_q| = 1/m \quad \text{and} \quad |\mathbf{b}_s|/|\mathbf{b}_q| = 1/n. \tag{2}$$

The one-fifth order spots of the reconstruction rows arranged around (0,0) can be used as internal calibration markers. From their distance $2b_{1/5}$ [see Fig. 2(b)], one obtains

$$|\mathbf{b}_q| = 5b_{1/5} - |\mathbf{b}_s|. \tag{3}$$

This relation holds not only for commensurate registries [15] but also for incommensurate ones as we have proved by means of LEED simulations based on the Moiré approach [63]. With Eq. (2), it follows that

$$m = (5b_{1/5} - |\mathbf{b}_s|)/|\mathbf{b}_l| \quad \text{and} \quad n = (5b_{1/5} - |\mathbf{b}_s|)/|\mathbf{b}_s|. \tag{4}$$

This finally gives $m = 13.1 \pm 0.5$ and $n = 60 \pm 3$. Hence, the Pt(001)-hex forms a $c(26.2 \pm 1.0 \times 120 \pm 6)$ superstructure based on the FFT evaluation of the STM data.

An even more distinct result is obtained if one postulates that the hex layer is forced by the substrate into a commensurate registry similar to that observed for the Au(001)-hex [63]. For that specific case, m and n are integers, and the diffraction spots of the hex are related to the reciprocal square lattice of Pt(001)-(1 × 1) in terms of rational numbers. Moreover, Van Hove *et al.* [15] have shown that for a commensurate

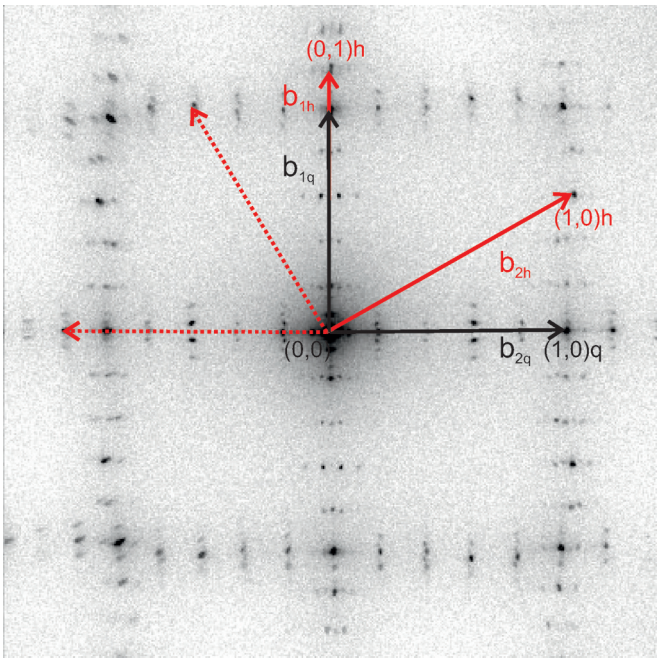

FIG. 3. The SPA-LEED pattern of the nonrotated Au(001)-hex for an electron energy of 220 eV. Reciprocal lattice vectors $\mathbf{b}_{1,2q}$ and $\mathbf{b}_{1,2h}$ of the Pt(001) substrate square lattice and the hex layer, respectively, are indicated by black and red arrows. The (0,1)*h* and (1,0)*h* diffraction spots of the hex and the (1,0)*q* spot of the square Pt(001) substrate are indicated in red and black, respectively. The dashed arrows demonstrate the presence of a second hex domain rotated by 90°.

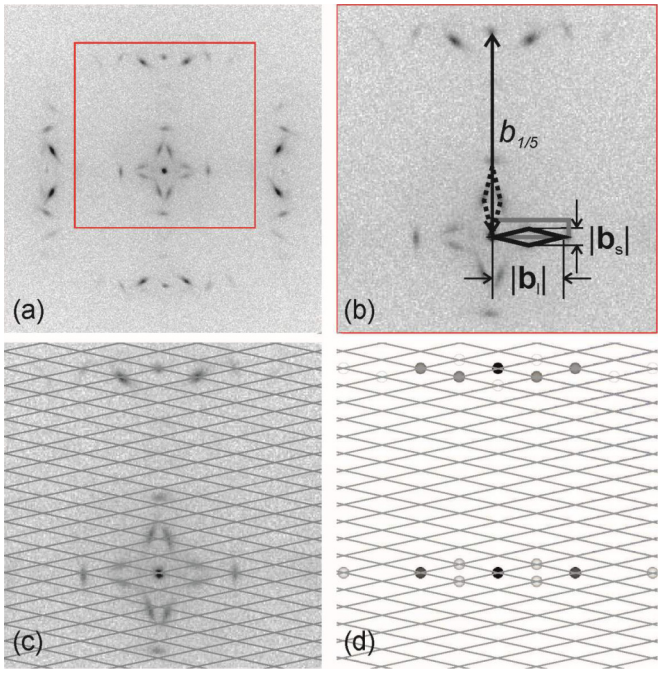

FIG. 4. (a) The SPA-LEED pattern of the nonrotated Pt(001)-hex around the central (0,0) spot, including the inner one-fifth spots of the reconstruction (200 eV). (b) and (c) Enlarged section marked in (a). A slight x-y asymmetry of (a) has been corrected by a vertical 3.9% expansion. (b) Measurement of structural parameters of the Pt(001)-hex is visualized. In the LEED pattern of (c), the diamondlike reciprocal lattice of the $c(26 \times 118)$ superstructure is superimposed for one domain. (d) Simulated $c(26 \times 118)$ LEED pattern. The simulated LEED spots are represented as gray dots in which the gray levels represent the intensity.

$c(2m \times 2n)$ structure, the relations

$$b_{1/5} = (n' + 1)|\mathbf{b}_s|, \quad \text{and} \quad n = 5n' + 4 \tag{5}$$

hold with $n\prime$ being also an integer. Therefore, assuming a commensurate hex superstructure from the values of $b_{1/5}$, $|\mathbf{b}_s|$, and $|\mathbf{b}_l|$ measured as indicated in Figs. 2(b) and 2(c), one is able to decide that $m = 13$ and $n = 59$. Consequently, the Pt(001)-hex reconstruction can be characterized by a centered $c(26 \times 118)$ superstructure. However, such a statement has to be handled with care. As already stressed, there is the uncertainty as to whether the observed structure is really representative for the entire surface. This can be decided only by applying integral diffraction experiments.

In our investigations, we rely on SPA-LEED [61,62] for high-resolving integral structure characterization. Figure 3 shows a SPA-LEED image of the Pt(001)-hex sample taken at 220 eV. As characteristic for SPA-LEED, all diffraction spots including the (0,0) spot are visible since shadowing effects due to the sample holder or the electron gun do not arise. The reciprocal unit vectors $\mathbf{b}_{1,2h}$ of the hex top layer and $\mathbf{b}_{1,2q}$ of the square (1×1) substrate are drawn as red and black arrows, respectively. As the LEED pattern characterizes the reconstruction structure of the whole sample, it sizes also the second domain, which is rotated by 90°. In Fig. 3, the lattice vectors of the 90° rotated domain are indicated by dashed red arrows. It is evident that $\mathbf{b}_{1h}$ is oriented exactly along the vector $\mathbf{b}_{1q}$ and that the spots of the hex domains such as the (0,1)*h* and (1,0)*h* ones are sharp. This clearly reveals that a nonrotated hex is present over the full sample area. Moreover, one observes groups of the characteristic extradiffraction spots of the hex reconstruction near one-fifth order positions of the spots of the square Pt(001)-(1×1) substrate lattice.

Figure 4(a) shows the vicinity of the central (0,0) LEED spot with the adjacent one-fifth order spots in higher resolution. On this enhanced scale, one clearly perceives that the LEED spots are arranged in diamondlike constellations, as it is characteristic for a centered rectangular unit cell. This clearly indicates that the hex structure cannot be described by primitive rectangular unit cells, as proposed previously [14,15,22]. Instead the SPA-LEED studies corroborate the STM measurements and reveal also a $c(2m \times 2n)$-like superstructure.

For a quantitative analysis of the diffraction pattern, i.e., for determining the m and n values, the inner area around (0,0) of the diffraction data, as marked in red in Fig. 4(a), has been considered. It is shown enlarged in Figs. 4(b) and 4(c). Hereby, the SPA-LEED induced image distortions have been corrected. Whereas the characteristic barrel distortion can be neglected for the (0,0) vicinity, a slight $x-y$ asymmetry of the measurement was compensated by a vertical 3.9% expansion of the image. In Fig. 4(b), the rhombic unit mesh of one hex domain is drawn in black lines together with the corresponding centered rectangular unit cell displayed in gray. The dashed lines shows the unit mesh of the other domain. The quantitative analysis follows the same procedure that has been

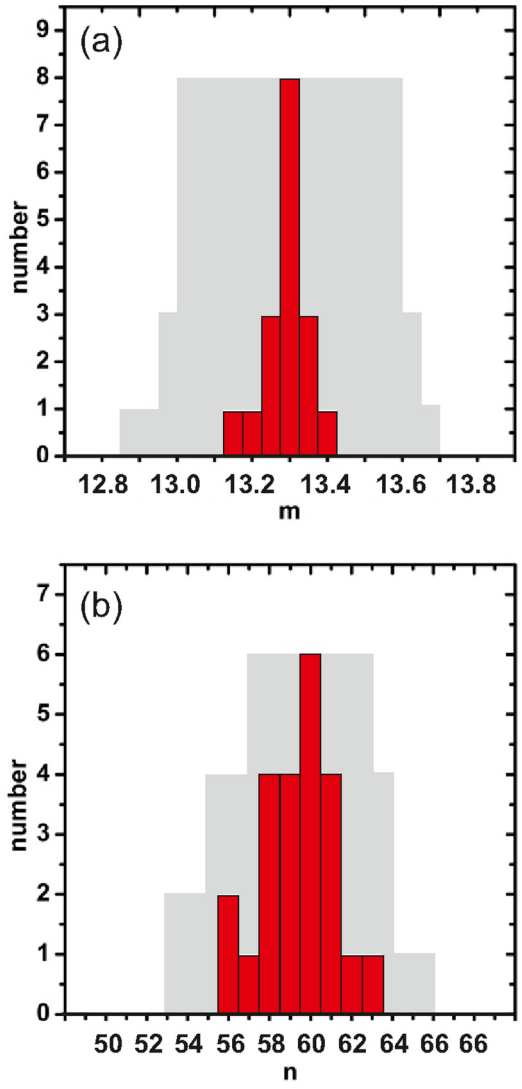

FIG. 5. Statistical evolution of the $c(2m \times 2n)$ unit cell determination for 17 different preparations of the Pt(001)-hex. (a), (b) Frequency of occurrence for the unit cell dimensions m and n, respectively. The areas of uncertainty are indicated in gray. For details, see text.

applied for the FFT of the STM measurement [see Figs. 2(b) and 2(c)]. The parameters $|\mathbf{b}_s|$,$|\mathbf{b}_l|$, and $b_{1/5}$ defining the hex superstructure have been determined, as visualized in Fig. 4(b) and evaluated by applying Eq. (4) for determining the m and n values. In detail, 17 measurements of different preparations of the Pt(001)-hex have been analyzed. In Fig. 5, the obtained m and n values are displayed in the form of bare graphs drawn together with their uncertainty ranges. The uncertainty of the measurements results from the uncertainty of the determination of the spot centers. The spots display an intensity distribution with a distorted Gaussian shape (mean peak half width about 0.7–1.1%$|\mathbf{a}_q|$ depending on preparation) mainly due to structural imperfections. Due to these distortions, the peak center can be determined only with a precision of about 2%. Considering this uncertainty, one deduces from Fig. 5 that $m \approx 13.28 \pm 0.30$ and $n \approx 59.3 \pm 3.0$. Within the error margins, the obtained m and n values correlate at least with the integers 13 and 59, respectively, which would indicate that

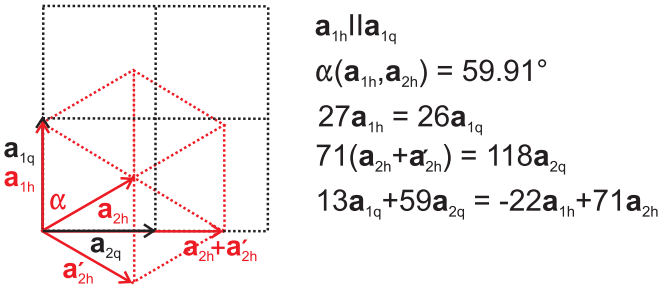

FIG. 6. Pt(001)-hex-$c(26 \times 118)$: Epitaxial relationships of the hex to the square substrate.

the Pt(001)-hex forms a commensurate $c(26 \times 118)$ structure. The attained precision definitely excludes any other form of a commensurate superstructure. Of course, this is not proof for the commensurate nature of the hex layer registration itself. Considering the dispersion ranges of m and n, an incommensurate structure such as a $c(26.6 \times 118)$ structure cannot be completely excluded. In any case, the commensurate $c(26 \times 118)$ structure can be considered as an adequate approximation to the real Pt(001)-hex structure.

In Fig. 4(c), the diamondlike lattice of one domain of the deduced $c(26 \times 118)$ superstructure is superimposed to the diffraction pattern. As one can see, the intersection points match well with the corresponding LEED spots.

Having established a $c(26 \times 118)$ superstructure of the Pt(001) reconstruction, the relation between the square substrate and the nearly hexagonal top layer is given by

$$13\mathbf{a}_{1q} + 59\mathbf{a}_{2q} = -22\mathbf{a}_{2h} + 71\mathbf{a}_{2h},$$

as visualized in Fig. 6. The real space lattice vectors $\mathbf{a}_{1h}$ and $\mathbf{a}_{2h}$ of the hex layer therefore amount to

$$\mathbf{a}_{1h}||\mathbf{a}_{1q}, \quad |\mathbf{a}_{1h}| = 0.9630|\mathbf{a}_{1q}|, \quad |\mathbf{a}_{2h}| = 0.9604|\mathbf{a}_{2q}|, \quad \text{and} \quad \alpha(\mathbf{a}_{1h},\mathbf{a}_{2h}) = 59.91^\circ, \tag{6}$$

where $\alpha(\mathbf{a}_{1h},\mathbf{a}_{2h})$ is the angle between both hex vectors. Hence, the hex is not homogeneously compressed. Whereas along [110] the compression amounts to 3.70%, perpendicular to that direction a 4.04% compression is established.

For a deeper backing of these findings, we performed a simulation of the corresponding LEED pattern. In the simulation, we analyzed the Moiré-like modulation of the hex layer by the quadratic Pt(001) substrate. This Moiré approach is based on the established fact that the Fourier plane image of the Moiré pattern formed by two periodic lattices can be described by a convolution of the two corresponding reciprocal lattices in reciprocal space [69]. Following this Moiré approach for the Pt(001)-hex, the positions $\mathbf{b}_{n,m,n',m'}$ of the diffraction spots can be determined by a linear combination of the reciprocal lattice vectors $\mathbf{b}_{1h}$ and $\mathbf{b}_{2h}$ of the hex top layer, as given by Eq. (1), and $\mathbf{b}_{1q}$ and $\mathbf{b}_{2q}$ of the quadratic Pt(001) substrate

$$\mathbf{b}_{m,n,m',n'} = m\mathbf{b}_{1q} + n\mathbf{b}_{2q} + m'\mathbf{b}_{1h} + n'\mathbf{b}_{2h}, \tag{7}$$

where m, n, m', and n' are integers [69].

To account for the expected decrease of the spot intensity I with the order of diffraction, an empirical *ad hoc* structure

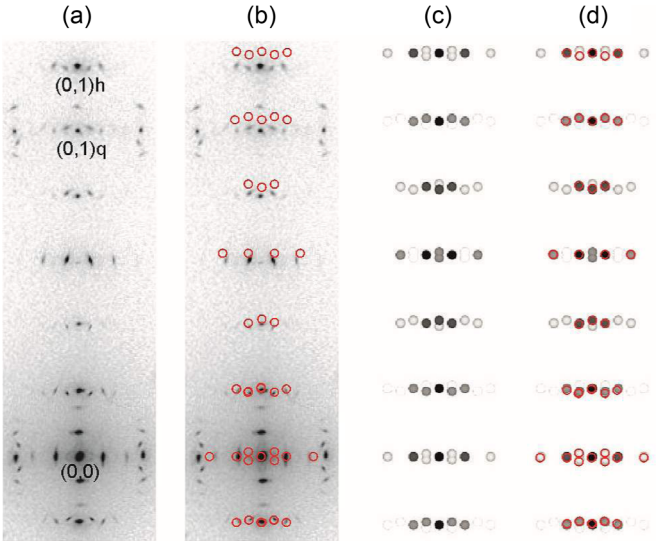

FIG. 7. The SPA-LEED pattern, (a) and (b), of a nonrotated Pt(001)-hex extending from (0,0) to (0,1)*h* spots (220 eV). (b) The SPA-LEED and for barrel distortion corrected spot positions (red circles). (c), (d) Simulated $c(26 \times 118)$ LEED pattern. The simulated LEED spots are represented as gray dots in which the gray levels represent the intensity. (d) Corrected experimental spot positions shown in (b) are superimposed.

factor has been included in the simulation by stating that

$$I = (m + n)^{-q},$$

where the exponent q was adapted to the measured intensities and ranged between 2 and 4.

In Fig. 4(d), the simulation results are displayed for one hex domain. The vicinity of the (0,0) spot is displayed with the same scale as the LEED image of Fig. 4(c). The simulated LEED spots are depicted as gray dots, where the gray levels roughly represent the spot intensities. In addition to that, a $c(26 \times 118)$ lattice is superimposed, similar as that in Fig. 4(c). As one can see, the Moiré approach yields an excellent agreement between the simulated and the measured diffraction pattern. Spots with noticeable intensities appear only in the vicinities of (0,0) and one-fifth order positions of the Pt(001)-(1×1) unit cell similar, as observed in the measurement. In addition, the simulation reproduces the measured spot positions.

For proving the results of the Moiré approach for higher order spots, an enlarged diffraction area, as displayed in Figs. 7(a) and 7(b), has been considered. It shows the diffraction pattern of the Pt(001)-hex extending between the (0,0) and the (0,1)*h* spot vicinities. For a direct comparison with the simulated diffraction pattern, the characteristic barrel distortion of SPA-LEED [66] influencing the larger diffraction angles has been corrected, as described below. For one domain, the corrected experimental spot positions are indicated in Fig. 7(b) as red circles. The results of the LEED simulation presupposing a $c(26 \times 118)$ superstructure are drawn in Figs. 7(c) and 7(d). As in Fig. 4(d), the simulated LEED spots are represented by gray dots, where the gray level indicates the intensity. In Fig. 7(d), the corrected spot positions of Fig. 7(b) are superimposed to the simulated ones. Again, the detailed agreement between simulated and measured diffraction patterns is remarkable. For the used energy of 220 eV, even the relations between the simulated spot intensities are in good accordance with the measurement. Hence, the simulation capacity of the Moiré approach has been strikingly confirmed also for higher order diffraction beams. Of course, this simulation aptness of the Moiré approach can be directly attributed to the Moiré-like nature of the Pt(001)-hex reconstruction itself. The latter has been realized already by Heinz *et al.* [70] who had shown that the main features of the diffraction pattern of the Pt(001)-hex can be explained by a simple double diffraction process occurring from a hexagonal surface layer and quadratic bulk layers. This has been proven in their study by an optical laser simulation where the diffracted laser beams of a hexagonal grating were sent through a second grating with quadratic structure.

B. Variants of rotated hexagonal top layers

Already in early investigations [12–14], it has been observed that the nonrotated Pt(001)-hex is only a metastable form of the Pt(001) reconstruction. At temperatures above 900 °C, a rotated hex is established showing rotation angles of $0.7^\circ \pm 0.2^\circ$. In our investigations, we were able to analyze with much higher precision the rotated variants of the hex. Starting with an annealing temperature slightly above the Pt(001)-hex formation temperature, e.g., at 970 °C, and increasing it up to 1170 °C, a clear change of the LEED pattern is induced. This is demonstrated by the SPA-LEED images compiled in Figs. 8(a)–8(c). The left column in Fig. 8 shows the diffraction pattern between the (0,1)*q* and the (0,1)*h* spots, whereas the middle and the right ones show the (0,0) spot vicinity in two different magnifications. Considering the (0,1)*h* spot first, one observes at temperatures around 920 °C [Fig. 8(a)] a streaklike blurring, whereas the spots of the quadratic substrate such as the (0,1)*q* one remain sharp. Inspecting the other hex spots (not shown here), one perceives that their blurring occurs in a bow-like manner on a circle around the central (0,0) spot. Similar to the case of the Au(001) reconstruction [63], this clearly indicates that the hex layer is continuously rotated over an angle range between -0.7° and $+0.7^\circ$. The even contrast level of the blurring streaks indicates that the rotation proceeds in a continuous form where no specific angles are favored.

Annealing the sample at temperatures around 1080 °C induces the appearance of three sharp hex spots [Fig. 8(b)]. The central spot indicates that domains are present that exactly reside in the nonrotated form on the Pt(001) substrate. The split spots, on the other hand, reveal that rotated hex domains are present, which are now locked in a fixed rotation angle of about 0.75°.

A final annealing at temperatures around 1170 °C yields exclusively the spots of the two rotated hex domains [Fig. 8(c)]. The vanishing of the central hex spot indicates that the nonrotated hex is not stable at elevated annealing temperatures. During this high temperature treatment, the rotation angle of both hex domains increases, as compared to the situation in Fig. 8(b), as the increased splitting distance of the hex spots indicates.

Inspecting the (0,0) spot vicinities [middle and right columns of Figs. 8(a)–8(c)], one perceives that the super-

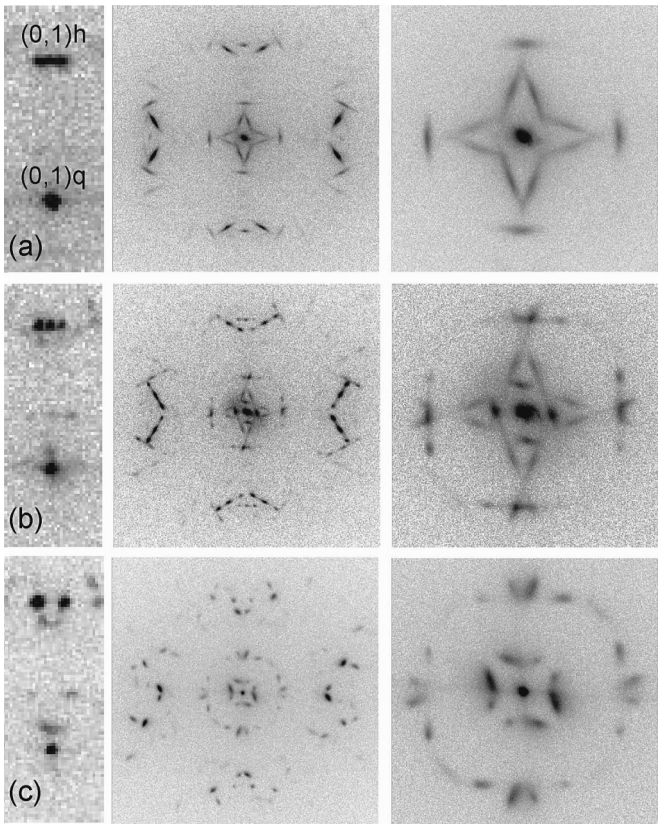

FIG. 8. The SPA-LEED patterns showing variants of the rotated Pt(001)-hex-R observed after annealing. Sections between the (0,1)q and (0,1)h spots (left) taken at 220 eV and the (0,0) vicinity, including the one-fifth order spots (middle) and the direct neighborhood of (0,0) spot (right) both taken at 200 eV, are displayed. Annealing temperatures (a) 920 °C, (b) 1080 °C, and (c) 1170 °C. For details see text.

structure spots also show the blurring and splitting effects, respectively. They occur, however, in a more complex manner on inclined tracks. This leads in the case of the continuous hex rotation to the formation of a starlike diffraction pattern around (0,0) [right image of Fig. 8(a)]. In addition, it is obvious that the superstructure spot constellations reflect the transformation of the (0,1)h spot on an enhanced scale. The starlike spot blurring, e.g., extends over an angle range, which is by almost a factor of 10 larger than the blurring of the hex spots.

For a quantitative understanding of the modification of the diffraction patterns induced by the hex layer rotation, again LEED pattern simulations using the Moiré approach proved beneficial in this paper. Similar to our former investigations of the hexagonal Au(001) reconstruction, we assumed that during rotation the internal lattice structure of the hex stays as defined for the nonrotated hex [see Eq. (6)]. The results of the simulation are displayed in Fig. 9 for the diffraction area around the (0,0) spot. The rotation was performed in angular steps of $\varphi = 0.1^\circ$. We start by considering a nonrotated single domain $c(26 \times 118)$ unit cell [blue diamond in Fig. 9(a)]. Rotating the rigid top layer in a clockwise manner in nine angle steps from 0° to 0.9° results in the diffraction pattern displayed in Fig. 9(b). The simulation of the rotation in Fig. 9(b) results in LEED spots that move on linear tracks

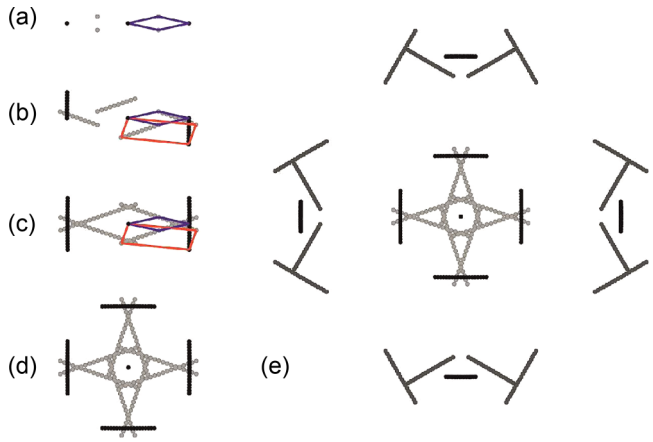

FIG. 9. Simulation of the diffraction pattern of the continuously rotating Pt(001)-hex-R. Rotation steps 0.1°. For one hex domain, the direct neighborhood of the (0,0) spot is shown in (a)–(c) for rotation angles of (a) 0°, (b) 0°–0.9°, and (c) 0°–±0.9°. (d) Simulated pattern of (c) is indicated for both domains. (e) Simulated diffraction pattern of both domains, including also the one-fifth order spots. Unit cells of the nonrotated hex and the 0.9° rotated hex are given in blue and red, respectively.

and form blurring streaks for a continuous rotation range in the same manner observed in the SPA-LEED images. During hex layer rotation, the initially rhombic unit cell transforms to a more rhomboidlike one. Including also a counterclockwise hex rotation, the simulation shown in Fig. 9(c) is obtained. The superposition of the spots of the second domain yields the complete diffraction pattern as displayed in Fig. 9(d). In Fig. 9(e), a larger diffraction area around (0,0) is shown, including also the neighboring one-fifth order spots. The simulated diffraction pattern fits perfectly to the measured one found for the continuously rotated hex, as shown in Fig. 8(a).

It is obvious that the spots of the initially rhombic unit cell of the nonrotated hex show a different behavior during hex layer rotation. The spots defining the long diameter of the rhomb (i.e., the $\mathbf{b}_l$ spots) move on relatively short tracks along the high symmetry directions of the Pt(001) substrate. The spots defining the short diameter of the rhomb (i.e., the $\mathbf{b}_s$ spots), on the other hand, move on inclined tracks and show much larger track widths than the $\mathbf{b}_l$ spots. That means that the $\mathbf{b}_s$ spots react most sensitively on the rotation. Hence, they can be used to extract with high precision the given rotation angle φ of the hex. This is visualized by the scheme presented in Fig. 10(a) showing again the tracking courses of the $\mathbf{b}_l$ and $\mathbf{b}_s$ spots during rotation. For defining the hex rotation angle, we determine the length w of the line tracks discussed above and indicated in Fig. 10(a). From the measured distance $2 \times |\mathbf{b}_l|$, one gets via Eqs. (2) its relation to $|\mathbf{b}_q|$. The ratio $w(\varphi)/|\mathbf{b}_q|$ scales sensitively with the corresponding rotation angle of the hex, as derived from the simulations and shown in Fig. 10(b). As an example, we analyze the measurement that is displayed in Fig. 10(c). Here the hex domains show at least three different rotation angles. This is indicated by the arrows marking the given ending points of the $\mathbf{b}_s$ tracks defining w. Relating it to the diagram of Fig. 10(b), one finds rotation angles of $0.770^\circ \pm 0.015^\circ$, $0.880^\circ \pm 0.015^\circ$, and $0.940^\circ \pm 0.015^\circ$, respectively. Note the attained high accuracy level of this SPA-LEED based

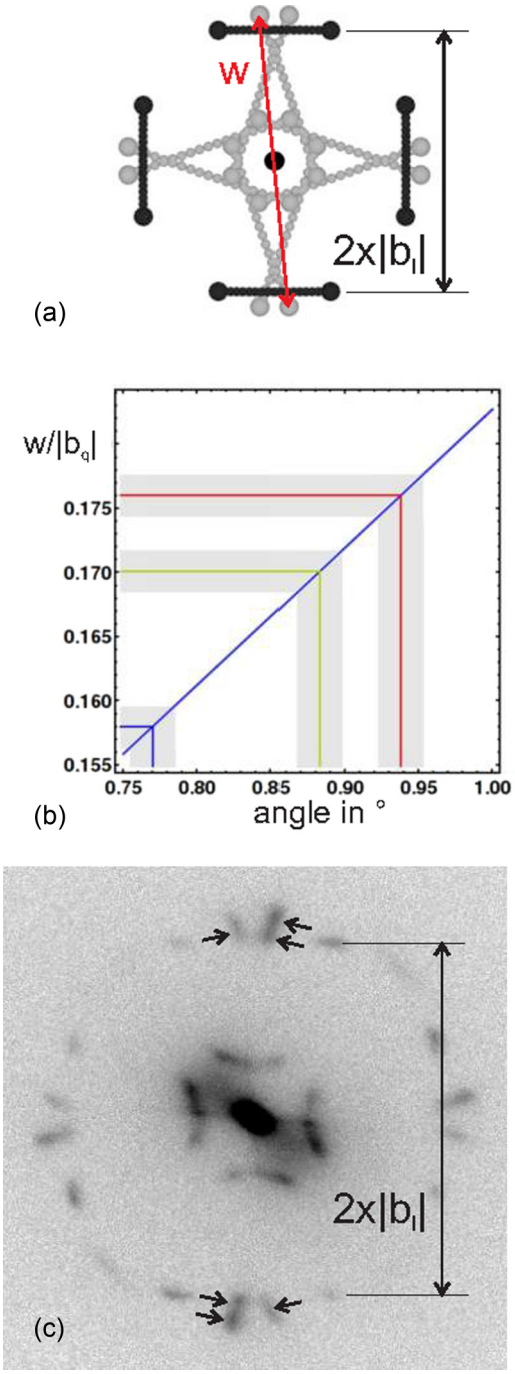

FIG. 10. (a) Scheme of the diffraction pattern and determination of the parameter $w(\varphi)$. (b) Angle dependence of $w(\varphi)$ as deduced from the LEED simulations. (c) The SPA-LEED pattern of the rotated Pt(001)-hex-*R* measured after a 1120 °C annealing (200 eV). The direct neighborhood of the (0,0) spot is displayed. Same image size as in the images shown in the right column of Fig. 8. For details, see text.

analysis. The rotation angles have been determined with a precision of 2%. The multitude of the found rotation angles indicates that for the analyzed sample preparation, the hex is not completely locked in the energetically most favored rotation state. The latter seems to be the 0.94° rotation, which more and more prevails at higher annealing temperatures, as the measurement of Fig. 8(c) indicates.

Up to now we have focused on the (0,0) surroundings for understanding the hex rotation induced changes of the LEED pattern. However, there are also distinct changes of the diffraction pattern appearing at larger diffraction angles. In Fig. 11, the simulated and the measured diffraction patterns for a larger diffraction area extending between the (0,0) to (0,1)*h* spots are displayed for the energetically favored rotation angle of 0.94°. Figure 11(a) shows in blue the positions of the simulated superstructure spots for a single hex domain rotated clockwise by 0.94°. The (0,1)*q* spot and the (0,1)*h* hex spots are displayed in red and green, respectively. This pattern is superimposed in Fig. 11(b) by the pattern of the anticlockwise rotated domain (yellow dots), which reveals the characteristic splitting of the hex spot (see arrows), whereas the (0,1)*q* spot stays in its position. In Fig. 11(c), the simulated diffraction spots are displayed in gray where the gray level represents the intensity. In Fig. 11(d), the measured SPA-LEED image of the rotated hex is displayed for comparison. It shows a larger diffraction area containing four split hex spots (green arrows). The detailed congruence between the measurement and the simulation is remarkable. Even the measured intensities are in good accordance with the simulations for the used diffraction energy of 220 eV.

The hex layer rotation shows that the nonrotated Pt(001)-hex, i.e., the commensurate $c(26 \times 118)$ structure, represents only a metastable form of the Pt(001) reconstruction. For specific hex rotation angles, more energetically favored registries of the hex to the square substrate exist. In order to understand this outcome, one has to consider the energetic balance within the hex-substrate system, which implies the interaction potentials E_{hex} within the hex and $E_{\text{hex-sub}}$ between the hex and the Pt(001) substrate, respectively. For cases where $E_{\text{hex-sub}} > E_{\text{hex}}$, one would certainly expect that a commensurate registry is the energetically most favored matching. However, the atomic interaction within the hex is considerable. Due to the relativistic enhancement of the *d*-*d* hybridization [44], a substantial compression effect is induced. This compression is so strong that it can reduce the interatomic distance within the hex by more than 4%. Hence, it works like a circular reinforcement that, on the one hand, stabilizes the internal hex structure even during hex rotation. On the other hand, the strong compression may cause the E_{hex} balance or even outbalance $E_{\text{hex-sub}}$. For other systems of strong interlayer interaction and large unit cells such as found for molecular films on metals, it has been recently shown that energetically favorable lattice structures are not restricted to commensurate ones [64,71,72]. There is also the possibility that film rotation induces a point-on-line matching of film and substrate where lattice lines of the film coincides with lattice lines of the substrate. This special type of epitaxy may induce minima in the film-substrate interaction potential. For the search of the parameters of point-on-line relationships, the inspection of the reciprocal space situation is useful. For such relationships, reciprocal lattice vectors of the film have to end on reciprocal lattice points of the substrate.

In order to more deeply understand the rotation of the Pt(001)-hex-$c(26 \times 118)$, we have tentatively adopted this new conception of epitaxy. A simple procedure has been developed, which allows finding coincidences of reciprocal lattice points of the hex and the square substrate in dependence

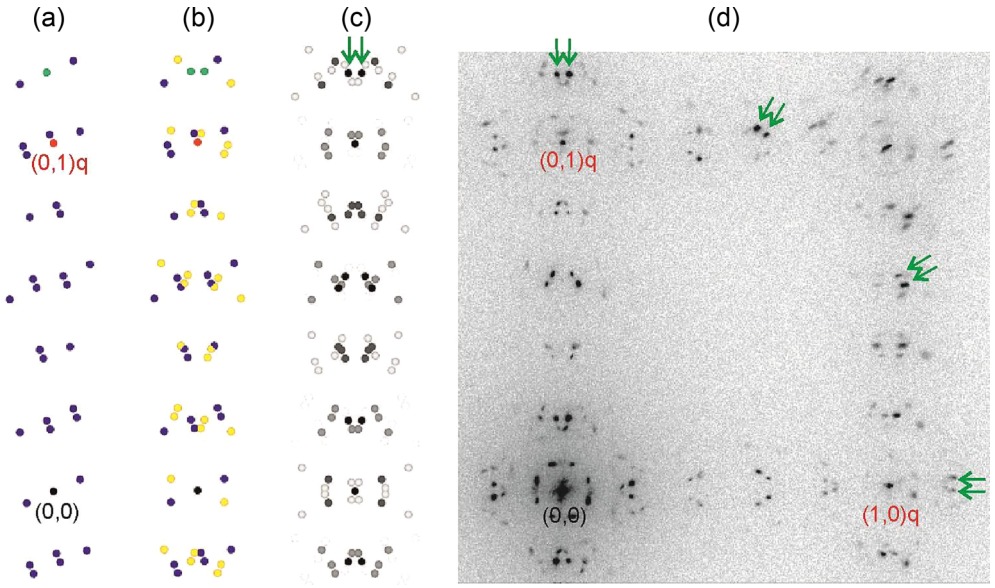

FIG. 11. (a)–(c) Simulated and (d) measured diffraction pattern of a Pt(001)-hex-*R* 0.94° extending from the (0,0) to the (0,1)*h* spot vicinities (220 eV). In the simulation, one domain is considered, which is in (a) rotated by +0.94° (blue spots) and in (b) by ±0.94° (blue and yellow spots). (c) The LEED spots of both rotation states are displayed by gray dots, which represent the diffraction intensity. The SPA-LEED image of (d) shows a larger diffraction area, including also the (1,1)*q* spot. The characteristic splitting of the hex spots is indicated by pairs of green arrows.

of the rotation angle. Several reciprocal lattice matchings events have been obtained, which include also coincidences for the found fixed rotation angles of 0.77°, 0.88°, and 0.94° (see Table I). Hence it seems that the concept of pol and lol epitaxy may help to elucidate the rotation behavior of the Pt(001)-hex. However, the numerical values (orders) of the coinciding reciprocal lattice points are relatively high, which indicates a rather marginal improvement of the energetic situation. We therefore also considered a slight lattice modification of the hex within the experimental error bars. That means besides the nonrotated $c(26 \times 118)$ low-temperature superstructure, we analyzed also the rotation of an incommensurable $c(26.6 \times 118)$ superstructure (see Fig. 5). However, the simulation yields no substantial improvement for the substrate registry if such a modified structure rotates. Certainly, there are also coinciding reciprocal lattice points for the observed rotation angles (see Table II). However, the numerical values are of a similar order as that found for the commensurable $c(26 \times 118)$ structure. Nevertheless, one has to keep in mind that such simple geometric considerations are clearly not sufficient for a deeper understanding of such complex reconstructions. The theoretical modeling of epitaxial supercells of more than 3000 atoms is needed here. Unfortunately, this is beyond the actual computational power of first principle calculations, which today sizes only cells with some 100 atoms [46].

TABLE I. Common reciprocal lattice points of the hex and the square substrate found for different rotation angles of the initial commensurate Pt(001)-hex-$c(26 \times 118)$.

n_{quad}	m_{quad}	n_{hex}	m_{hex}	φ
9	26	9	17	0.77°
35	47	33	23	−0.88°
8	45	7	34	−0.93°

TABLE II. Common reciprocal lattice points of the hex and the square substrate found for different rotation angles of the initial incommensurate Pt(001)-hex-$c(26.6 \times 118)$.

n_{quad}	m_{quad}	n_{hex}	m_{hex}	φ
29	4	28	−11	0.77°
44	27	42	2	−0.88°
8	45	7	34	−0.93°

IV. SUMMARY

By applying STM and SPA-LEED combined with LEED simulations based on the Moiré approach, we present a high-resolution study of the hexagonal reconstruction of Pt(001). Annealing to 850 °C yields the formation of a hexagonal top layer where closed packed atomic rows follow the [110]-like directions of the square Pt(001)−(1 × 1) substrate. This nonrotated hex approaches a Moiré-like $c(26 \times 118)$ superstructure, which is in commensurate registry with the quadratic substrate. However, experimental uncertainties cannot fully rule out an incommensurate $c(26.6 \times 118)$ superstructure. Sample annealing at 920 °C yields a continuous rotation of the hex layer between an angle area of −0.7° and +0.7°. Within this angle area, no favored rotation angles were observed. During rotation, the internal structure of the $c(26 \times 118)$ hex is maintained due to its strong internal compression. Annealing around 1080 C establishes fixed rotation angles of 0.77°, 0.88°, and 0.94°, which may partly coexist even together with the nonrotated hex. For temperatures around 1170 °C, the rotated Pt(001)-hex-*R* 0.94° is identified as the energetically most

favored reconstruction structure of Pt(001). It is described as an incommensurate structure that might have a point-on-line registry with the Pt(001) substrate. However, for a deeper understanding of the observed Pt(001)-hex formation and rotation, one has to await large-scale theoretical treatment that is not available today.

ACKNOWLEDGMENTS

Financial support by the Deutsche Forschungsgemeinschaft Sonderforschungsbereich 762 "Functionality of Oxidic Interfaces" is gratefully acknowledged. The authors would like to thank R. Kulla for technical support.

[1] S. Hangstrom, H. B. Lyon, and G. A. Somorjai, Phys. Rev. Lett. **15**, 491 (1965).
[2] D. G. Fedak and N. A. Gjostein, Phys. Rev. Lett. **16**, 171 (1966).
[3] D. G. Fedak and N. A. Gjostein, Surf. Sci. **8**, 77 (1967).
[4] P. W. Palmberg and T. N. Rhodin, Phys. Rev. **161**, 586 (1967).
[5] A. M. Mattera, R. M. Goodman, and G. A. Somorjai, Surf. Sci. **7**, 26 (1967).
[6] J. T. Grant, Surf. Sci. **18**, 228 (1969).
[7] A. Ignatiev, A. V. Jones, and T. N. Rodin, Surf. Sci. **30**, 573 (1972).
[8] F. Grønlund and P. E. Højlund Nielsen, J. Appl. Phys. **43**, 3919 (1972).
[9] G. E. Rhead, J. Phys. F: Met. Phys. **3**, L53 (1973).
[10] D. M. Zehner, B. R. Appleton, T. S. Noggle, J. W. Miller, J. H. Barret, L. H. Jenkins, and E. Schow III, J. Vac. Sci. Technol. **12**, 454 (1975).
[11] T. N. Rhodin and G. Brodén, Surf. Sci. **60**, 466 (1976).
[12] J. F. Wendelken and D. M. Zehner, Surf. Sci. **71**, 178 (1978).
[13] H. Melle and E. Menzel, Z. Naturforsch. A **33A**, 282 (1978).
[14] P. Heilmann, K. Heinz, and K. Müller, Surf. Sci. **83**, 487 (1979).
[15] M. A. Van Hove, R. J. Koestner, P. C. Stair, J. P. Biberian, L. L. Kesmodel, I. Bartos, and G. A. Somorjai, Surf. Sci. **103**, 189 (1981).
[16] K. Heinz, E. Lang, K. Strauss, and K. Müller, Surf. Sci. **120**, L401 (1982).
[17] K. Heinz, E. Lang, K. Strauss, and K. Müller, Appl. Surf. Sci. **11/12**, 611 (1982).
[18] E. Lang, K. Müller, K. Heinz, M. A. Van Hove, R. J. Koestner, and G. A. Somorjai, Surf. Sci. **127**, 347 (1983).
[19] W. Moritz, Analyse von Oberflächenstrukturen mit großen Einheitszellen und modulierten Überstrukturen durch Beugung niederenergetischer Elektronen, Habilitationsschrift Ludwig-Maximilians-Universität, München, 1983.
[20] N. Bickel and K. Heinz, Surf. Sci. **163**, 435 (1985).
[21] Y.-F. Liew and G.-C. Wang, Surf. Sci. **227**, 190 (1990).
[22] K. Mase and Y. Murata, Surf. Sci. **277**, 97 (1992).
[23] K. Johnson, Q. Ge, S. Titmuss, and D. A. King, J. Chem. Phys. **112**, 10460 (2000).
[24] A. Schmidt, W. Meier, L. Hammer, and K. Heinz, J. Phys.: Condens. Matter **14**, 12353 (2002).
[25] D. Gibbs, B. M. Ocko, D. M. Zehner, and S. G. J. Mochrie, Phys. Rev. B **42**, 7330 (1990).
[26] D. L. Abernathy, S. G. J. Mochrie, D. M. Zehner, G. Grübel, and D. Gibbs, Phys. Rev. B **45**, 9272 (1992).
[27] K. H. Rieder, T. Engel, R. H. Swendsen, and M. Manninen, Surf. Sci. **127**, 223 (1983).
[28] K. Kuhnke, K. Kern, G. Comsa, and W. Moritz, Phys. Rev. B **45**, 14388 (1992).
[29] G. Binnig, H. Rohrer, C. Gerber, and E. Stoll, Surf. Sci. **144**, 321 (1984).
[30] R. J. Behm, W. Hösler, E. Ritter, and G. Binnig, Phys. Rev. Lett. **56**, 228 (1986).
[31] A. Borg, A.-H. Hilmen, and E. Bergene, Surf. Sci. **306**, 10 (1994).
[32] G. Ritz, M. Schmid, P. Varga, A. Borg, and M. Rønning, Phys. Rev. B **56**, 10518 (1997).
[33] D. M. Kolb, Surf. Sci. **500**, 722 (2002).
[34] G. Lehmpfuhl and Y. Uchida, Surf. Sci. **235**, 295 (1990).
[35] N. Wang, Y. Uchida, and G. Lehmpfuhl, Surf. Sci. **284**, L419 (1993).
[36] N. Wang, Y. Uchida, and G. Lehmpfuhl, Surf. Sci. **296**, L1 (1993).
[37] K. Yamazaki, K. Takayanagi, Y. Tanishiro, and K. Yagi, Surf. Sci. **199**, 595 (1988).
[38] D. N. Dunn, J. P. Zhang, and L. D. Marks, Surf. Sci. **260**, 220 (1992).
[39] H. W. Zandbergen, C. W.-Pao, and D. J. Srolovitz, Phys. Rev. Lett. **98**, 036103 (2007).
[40] J. Witt and K. Müller, Phys. Rev. Lett. **57**, 1153 (1986).
[41] W. Telieps, M. Mundschau, and E. Bauer, Surf. Sci. **225**, 87 (1990).
[42] F. Ercolessi, E. Tosatti, and M. Parrinello, Phys. Rev. Lett. **57**, 719 (1986).
[43] B. W. Dodson, Phys. Rev. B **35**, 880 (1987).
[44] N. Takeuchi, C. T. Chan, and K. M. Ho, Phys. Rev. B **43**, 14363 (1991).
[45] Q. Ge, D. A. King, N. Marzari, and M. C. Payne, Surf. Sci. **418**, 529 (1998).
[46] P. Havu, V. Blum, V. Havu, P. Rinke, and M. Scheffler, Phys. Rev. B **82**, 161418(R) (2010).
[47] M. P. Cox, G. Ertl, and R. Imbihl, Phys. Rev. Lett. **54**, 1725 (1985).
[48] G. C. Bond, C. Louis, and D. T. Thompson, *Catalysis by Gold* (Imperial Collage Press, London, 2006).
[49] H.-J. Freund and G. Pacchioni, Chem. Soc. Rev. **37**, 2224 (2008).
[50] D. M. Kolb, Prog. Surf. Sci. **51**, 109 (1996).
[51] C. A. Lucas, P. Thompson, M. Cormack, A. Brownrigg, B. Fowler, D. Strmcnik, V. Stamenkovic, J. Greeley, A. Menzel, H. You, and N. M. Markovic, J. Am. Chem. Soc. **131**, 7654 (2009).
[52] M. Moiseeva, E. Pichardo-Pedrero, G. Beltramo, H. Ibach, and M. Giesen, Surf. Sci. **603**, 670 (2009).
[53] B. Voigtländer, G. Meyer, and N. M. Amer, Phys. Rev. B **44**, 10354 (1991).
[54] O. Fruchart, M. Klaua, J. Barthel, and J. Kirschner, Phys. Rev. Lett. **83**, 2769 (1999).
[55] K. Heinz and L. Hammer, Progr. Surf. Sci. **84**, 2 (2009).
[56] S. Günther, E. Kopatzki, M. C. Bartelt, J. W. Evans, and R. J. Behm, Phys. Rev. Lett. **73**, 553 (1994).
[57] M. Nomura and X.-Q. Wang, Phys. Rev. Lett. **81**, 2739 (1998).

[58] J. J. Mortensen, T. R. Linderoth, K. W. Jacobsen, E. Lægsgaard, I. Stensgaard, and F. Besenbacher, Surf. Sci. **400**, 290 (1998).
[59] C. Bombis and H. Ibach, Surf. Sci. **564**, 201 (2004).
[60] A. Trembulowicz, G. Ehrlich, and G. Antczak, Phys. Rev. B **84**, 245445 (2011).
[61] M. Henzler, Appl. Surf. Sci. **11/12**, 450 (1982).
[62] M. Horn-von Hoegen, Z. Kristallogr. **214**, 591 (1999); **214**, 684 (1999).
[63] R. Hammer, A. Sander, S. Forster, M. Kiel, K. Meinel, and W. Widdra, Phys. Rev. B **90**, 035446 (2014).
[64] S. C. B. Mannsfeld, K. Leo, and T. Fritz, Phys. Rev. Lett. **94**, 056104 (2005).
[65] R. J. Behm, P. A. Thiel, P. R. Norton, and G. Ertl, J. Chem. Phys. **78**, 7437 (1983).
[66] F. Sojka, M. Meissner, C. Zwick, R. Forker, and T. Fritz, Rev. Sci. Instrum. **84**, 015111 (2013).
[67] S. Foerster, M. Huth, K.-M. Schindler, and W. Widdra, J. Chem. Phys. **135**, 104701 (2011).
[68] T. Matsumoto, M. Batzill, H. Hsieh, and B. E. Koel, Surf. Sci. **572**, 146 (2004).
[69] I. Amidror, *The Theory of the Moiré Phenomenon: Vol. I, Periodic Layers* (Springer, London, 2009).
[70] K. Heinz, P. Heilmann, and K. Müller, Z. Naturforsch. A **32**, 28 (1977).
[71] M. Kiel, K. Duncker, C. Hagendorf, and W. Widdra, Phys. Rev. B **75**, 195439 (2007).
[72] C. Wagner, R. Forker, and T. Fritz, J. Phys. Chem. Lett. **3**, 419 (2012).